SPACE TELESCOPE SCIENCE INSTITUTE
Operated for NASA by AURA

Instrument Science Report COS 2023-11(v1)

Mitigation of the Fixed Pattern Noise on COS: Effective Signal-to-Noise versus Number of FP-POS Spectral Dithers

Julia Roman-Duval[1], Christian I. Johnson[1], Sten Hasselquist[1], Bethan James[1], Marc Rafelski[1], David Sahnow[1]

[1] Space Telescope Science Institute, Baltimore, MD

May 18, 2023

ABSTRACT

High-frequency variations in the flat-field of the COS FUV detector result in fixed-pattern noise that limits the signal-to-noise achievable by the instrument. The effects of fixed-pattern noise can be reduced via spectral dithering by utilizing multiple FP-POS positions, which correspond to one motor step rotation of the optical select mechanism. There are four FP-POS offsets available for each central wavelength. Here, we measure the maximum achievable S/N, $(S/N)_{\rm max}$, as a function of the number of FP-POS included in COS spectra for each segment and cenwave of the G130M, G160M, and G140L gratings. We use deep calibration observations aimed at measuring the two-dimensional spectral profiles of the different COS observing modes at LP3 to estimate the fixed pattern noise and resulting limiting S/N. As expected, we find that $(S/N)_{\rm max}$ increases as the number of FP-POS used increases. $(S/N)_{\rm max}$ also varies with wavelength (i.e., across a segment), grating, and cenwave. This variation can be attributed to changes in the width of the cross-dispersion profile. For settings or detector regions with wider cross-dispersion profiles, the fixed pattern noise is averaged over a larger number of two-dimensional pixels, resulting in a lower level of fixed pattern noise in extracted, one-dimensional spectra. With G130M, users can reach S/N of about 25, 30, and 35 with 2, 3, and 4 FP-POS, respectively. With G160M, users can expect to reach

S/N of 22, 28, and 32 with 2, 3, and 4 FP-POS, respectively. And with G140L, a maximum S/N of 23, 29, and 36 can be reached with 2, 3, and 4 FP-POS, respectively. Users are encouraged to use as many FP-POS as allowed by science requirements in order to maximize the legacy value of their data.

Contents

- Introduction (page 2)
- Observations and Methodology (page 4)
- Results (page 5)
- Summary and Conclusion (page 8)
- Change History (page 21)
- References (page 21)

1. Introduction

The Cosmic Origins Spectrograph (COS) far-ultraviolet (FUV) channel uses a combination of a photo-cathode and micro-channel plate (MCP) detectors to convert incoming photons into clouds of electrons. With three stacked MCPs operating with a high-voltage across them, each photon typically results in several million electrons at the bottom of the stack (Osterman et al. 2011). Cross-delay line (XDL) anodes located at the bottom of the MCPs measure the time and location of incident photons, as well as the number of electrons in the electron clouds, called the pulse height (PH) or gain.

The detector's quantum efficiency (QE) is improved by the presence of a series of wires (the QE grid or grid wires). The grid wires are placed above the detector (in the light path) and create shadows in the spectrum (Osterman et al. 2011). The grid wires are aligned with the cross-dispersion direction. As a result, their effect on 1D spectra does not vary with Y position on the detector. Additionally, the MCP's fiber bundles are assembled in a hexagonal pattern. The combination of the grid-wires and the "hex" pattern results in the flat-field shown in Figure 1, which is reproduced from Figure 5.13 of the COS instrument handbook (version 15).

While the grid-wire shadows and the low-frequency flat-field variations are corrected for in the CalCOS data reduction pipeline via a lifetime-position and grating dependent one-dimensional flat-field as part of the FLATCORR correction, the high-frequency flat variations (or P-flat) are not corrected for and result in fixed-pattern noise that limits the maximum achievable effective signal-to-noise (S/N, Ake et al. 2010). The fixed-pattern noise can be mitigated via spectral dithering, whereby different exposures are slightly offset along the dispersion direction. As a result, high-frequency

detector flat variations are averaged between different exposures, resulting a in reduced net fixed pattern noise.

Spectral dithering can be achieved through the use of different central-wavelength settings or fixed pattern positions (FP-POS), which are the minimal unit of spectral dithering corresponding to one step of the optical select mechanism 1 (OSM1, Osterman et al. 2011). The former results in different wavelength coverage, spectral resolution, and added overhead. The use of different FP-POS minimizes overhead, differences in spectral resolution (there is no focus adjustment between different FP-POS), and differences in wavelength coverage. There are four FP-POS settings available for each central wavelength (cenwave). Cenwaves are typically separated by 5 steps (e.g., 1291 — 1327 cenwaves for G130M, 1577—1623 cenwaves for 1623), which limits the number of FP-POS for each cenwave to four.

The use of all four FP-POS was required under most circumstances in order to maximize the S/N and archival legacy value of COS observations, as well as dither over bad detector pixels that can result in gaps in wavelength coverage. For grating/cenwaves combinations that place Lyman-α airglow on the FUVB detector, FP-POS dithering also helped spread gain-sag across the detector. Starting on October 2017 with the move to lifetime position 4 (LP4), the usage policy changed (see COS2025 policies[1] and Oliveira et al. 2018), restricting the use of G130M cenwaves and FP-POS in order to concentrate detector gain-sag linked to Lyman-α airglow into one new detector gap and extend the lifetime of COS (by a factor of roughly three). For all grating/cenwave combinations that did not place Lyman-α airglow on FUVB, the use of four FP-POS became even more essential so as to dither over this new detector gap incurred by gain-sag. We note that this new gap is not a physical gap such as the one that exists between segments A and B, but rather a very wide dead detector spot that is created by accumulated Ly-α airglow and subsequent gain-sag.

However, the move of G160M to LP6 in October 2022 was accompanied by significantly increased overheads associated with the use of multiple FP-POS owing to the new wavelength calibration approach called SPLIT-WAVECALS (James et al. 2023a). At LP6, wavelength calibration exposures cannot be taken concurrently with science exposures at LP6 owing to a light leak of the Pt-Ne lamp through the flat-field aperture (FCA, see Oliveira et al. 2013). Therefore, wavelength calibration of science exposures at LP6 requires separate lamp flashes performed before and after science exposures at a different aperture position not affected by the light leak (James et al. 2023b). As a result of these added overheads, the usage policy for FP-POS dithers had to be re-thought, taking into account the trade-off between the maximum achievable S/N and wavelength coverage for a given combination of FP-POS and the associated overhead (Hasselquist et al., 2023, in prep).

In this ISR, we estimate the maximum achievable S/N as a function of the number of FP-POS used for a given observation with a given cenwave. This work informs the FP-POS usage policy at LP6, which is the subject of a separate ISR (Hasselquist et al.,

[1] https://www.stsci.edu/hst/instrumentation/cos/proposing/cos2025-policies

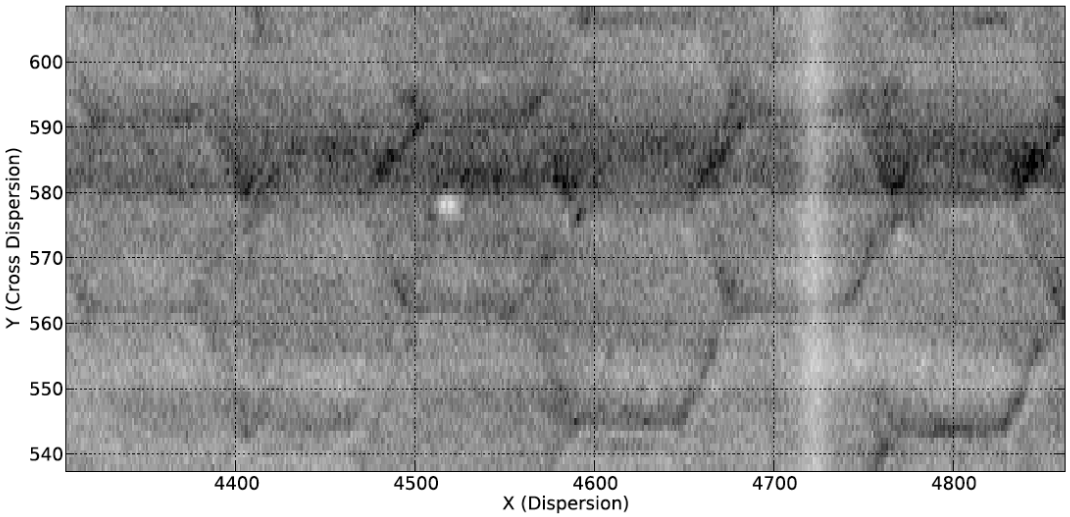

Figure 1. Flat-field of the FUV COS detector taken from Figure 5.13 of the Instrument Handbook version 15. A section of the FUV flat field showing representative detector features and a grid wire (the light vertical stripe at a pixel position of 4720).

2023, in prep). We use high S/N calibration data of flux standards (WD0308-565) for deriving the cross-dispersion profiles used for two-zone spectral extraction (Proffitt et al. 2015, Rafelski et al. 2018). Section 2 presents the observations and methodology used for this analysis. In Section 3, we present the results of the analysis, in particular how the maximum achievable S/N depends on the number of FP-POS included in the spectra, segment, grating, and cenwave. We summarize and conclude the analysis in Section 4.

2. Observations and Methodology

In order to evaluate the maximum effective S/N achievable for a given combination of FP-POS, the observations must match two requirements. First, the Poisson S/N of the data needs to exceed the maximum achievable effective S/N we are trying to measure (which we expect is of order 40-50). Second, the observations must target a continuum target, such as a flux standard white dwarf, in order to enable an accurate measurement of the S/N that is not impacted by interstellar or stellar absorption or emission lines. The calibration observations obtained to derive two-dimensional spectral profiles match those requirements. In particular, calibration program 13932 targeted white dwarf WD0308-565 with the G130M, G160M, and G140L gratings at LP3 with a Poisson S/N of $\sim$50 for the combined four FP-POS exposures. Observations taken at LP3 were not subject to the COS2025 policy and have the benefits of including FUVA and FUVB for all G130M cenwaves except the ”blue” modes operated at LP2 (i.e., 1222, 1291, 1300, 1309, 1318, 1327) and G160M cenwaves (1577, 1589, 1600, 1611, 1623) except for the

more recent 1533 setting. Additionally, cenwave 800 of the G140L was implemented in 2018 after the move to LP4 and is therefore not included in program 13932. This setting was later moved back to LP3 in 2022, and calibration data to create two-dimensional spectral profiles were obtained as part of program 16466. We therefore use G140L/800 data from program 16466 to measure the maximum achievable S/N with this setting.

For each possible combination of N FP-POS where N = 2,3, or 4, association files are re-created to include only the x1d files that are part of this combination. For two FP-POS settings, there are six possible combinations (1+2, 1+3, 1+4, 2+3, 2+4, 3+4). For 3 FP-POS settings, there are four possible combinations (1+2+3, 1+2+4, 1+3+4, 2+3+4). And there is of course only one combination of four FP-POS (1+2+3+4). Each association file corresponding to each possible combination is re-processed using CalCOS. For the older data from program 13932 (G130M; G160M; G140L/1105 and 1280), the calibration was performed by CalCOS version 3.3.9 (HSTDP 2019_6, caldp_20200323). For the more recent G140L observations with cenwave 800, CalCOS version 3.4.4 was used (HSTDP 2022_3, caldp_20221010). This resulted in *x1dsum* files for each combination of FP-POS, which is the co-added spectrum from *x1d* files corresponding to this combination of FP-POS.

The *flux* and *error* arrays in the *x1dsum* files are smoothed with a Box kernel of width 7 pixels in order to estimate the flux and error per resolution element (resel). The error array is also divided by $\sqrt{7}$ to estimate the Poisson noise per resel. We refer to those flux and Poisson error arrays as f_7 and e_7, respectively. The Poisson S/N is given by f_7/e_7. We choose to estimate the S/N per 7 pixel bin because the FWHM of the COS LSFs at LP3 is measured to be 7-8 pixels (Roman-Duval et al. 2017), which is higher than the standard 6 pixel resel assumed in the ETC.

Furthermore, the *flux* array of the *x1dsum* spectra is heavily smoothed by a box kernel of width 201 pixels in order to estimate a "noiseless" version of the flux (f_{201}), thanks to the fact that the spectrum of the flux standard is very smooth. However, in the G130M spectra, wide regions around interstellar absorption lines biasing the flux has to be masked out of these heavily smoothed spectra. Those regions are 1188 —1223 Å, 1258 —1264 Å, 1275 — 1281 Å, 1300 — 1310 Å, 1321 — 1326 Å, and 1332 — 1339 Å. The empirical noise $e_{\rm eff}$, which results from a combination of Poisson and fixed pattern noise, is then computed by applying a rolling standard deviation with a kernel of width 201 pixels to the difference $f_{201} - f_7$. The empirical S/N is finally estimated as $f_{201}/e_{\rm eff}$.

3. Results

The empirical (effective) S/N is plotted as a function of wavelength for the G130M/1291/FUVA setting and for combinations of 2 FP-POS in Figure 2 (this Figure is enlarged and allows more details to be discerned). Figures 3, 4 and 5 include all G130M cenwaves and both segments for 2, 3, and 4 FP-POS, respectively. Histograms of the empirical S/N combining all cenwaves for each segment and number of FP-POS (2, 3, 4) are shown in

Table 1. Maximum achievable S/N with COS/FUV

Grating	Segment	Percentile	2 FP-POS	3 FP-POS	4 FP-POS
G130M	FUVA	16^{th}	15	19	22
		50^{th}	22	27	32
		84^{th}	28	34	40
	FUVB	16^{th}	21	28	32
		50^{th}	27	34	40
		84^{th}	33	41	48
G160M	FUVA	16^{th}	14	18	21
		50^{th}	20	25	29
		84^{th}	25	32	37
	FUVB	16^{th}	17	24	27
		50^{th}	24	31	35
		84^{th}	30	37	43
G140L	FUVA	16^{th}	17	21	28
		50^{th}	23	29	36
		84^{th}	30	37	45

Figure 6. Similarly for G160M, the effective S/N as a function of wavelength is shown in Figures 7, 8 and 9 for 2, 3, and 4 FP-POS, respectively. The histogram of the effective S/N for 2, 3, and 4 FP-POS is shown in Figure 10. The results for G140L are shown in Figures 11, 12 and 13 for 2, 3, and 4 FP-POS, respectively, while the histograms of the maximum achievable S/N with G140L are shown in Figure 14. For all FUV gratings, the $16^{\rm th}$, $50^{\rm th}$, and $84^{\rm th}$ percentiles of these histograms are reported in Table 1.

For all settings used in this investigation, the Poisson S/N is above the effective S/N, indicating that the observations used in this analysis were deep enough that they could probe the maximum achievable effective S/N with COS/FUV gratings. Note that we attempted this analysis with the G130M/1222 cenwave, but the Poisson S/N on FUVB was not sufficient to probe the fixed pattern noise. Indeed, the effective and Poisson S/N were in nearly perfect agreement. Additionally, for G140L, the Poisson S/N drops at longer wavelengths. As a result, the Poisson S/N and effective S/N are roughly identical above 1700 Å, indicating that the S/N is limited by Poisson noise, not fixed pattern noise. We therefore do not include wavelengths above 1700 Å in this analysis for G140L.

As expected, for all segments, gratings and cenwaves, the maximum achievable S/N, which we will refer to as $(S/N)_{\rm max}$ in the rest of this ISR, increases as more FP-POS spectral dithers are combined. We do not find any differences in $(S/N)_{\rm max}$ between different combinations of the same number of FP-POS. In addition, $(S/N)_{\rm max}$ varies across each segment, and between segments, cenwaves and gratings. It is generally higher on FUVB than on FUVA for G130M and G160M, though the difference between FUVA and FUVB for G160M is smaller than for G130M. $(S/N)_{\rm max}$ is significantly higher for G130M than for G160M, and higher for G140L than for G130M.

The underlying reasons for these trends has to do with how the width of the cross-dispersion (XD) profiles depend on wavelength, grating and cenwave (see Figure 5.9 of the IHB). The wider the XD profile, the more fixed pattern noise is averaged out through spectral extraction, which involves summing counts along detector columns. As a result, $(S/N)_{\rm max}$ is higher in detector regions and grating/cenwave combinations with wider XD profiles. Since the XD profile of G130M is about twice as wide as G160M, $(S/N)_{\rm max}$ is higher for G130M than for G160M. Similarly, the XD width for G130M is higher on FUVB than on FUVA due to its intrinsic wavelength variations, and $(S/N)_{\rm max}$ is correspondingly higher on FUVB. The XD width of G140L varies significantly across FUVA, but it can generally exceed the width of G130M, resulting in a higher $(S/N)_{\rm max}$ for G140L than for G130M. While the Poisson S/N of the observations with the G130M/1222 setting is not sufficient to measure the fixed pattern noise, we expect that, owing to the wider XD profile of the 1222 cenwave, $(S/N)_{\rm max}$ is even higher for this setting.

To capture these variations of $(S/N)_{\rm max}$, we report in Table 1 the $16^{\rm th}$, $50^{\rm th}$, and $84^{\rm th}$ percentiles of the distribution of $(S/N)_{\rm max}$ for each grating/segment combination. Taking the $50^{\rm th}$ percentile values of $(S/N)_{\rm max}$ averaged over FUVA and FUVB for each grating as a rough estimate of the maximum achievable S/N, we find that, with G130M, users can reach S/N of about 25, 30, and 35 with 2, 3, and 4 FP-POS, respectively.

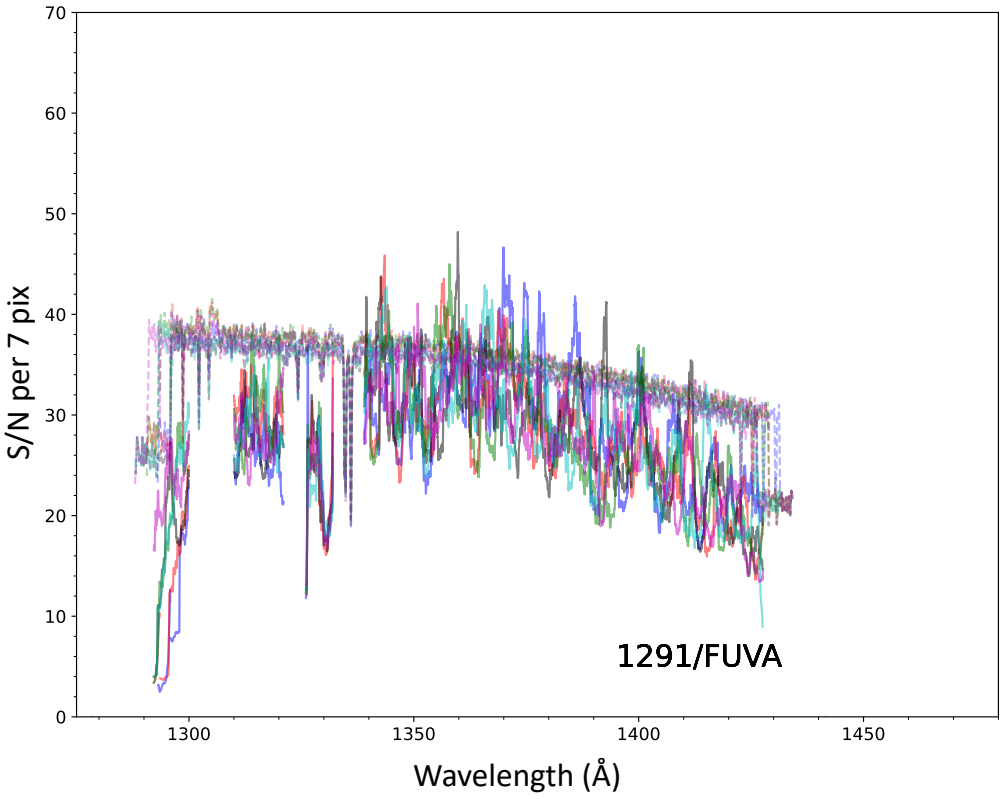

Figure 2. Empirical (effective) S/N per 7 pixel resel as a function of wavelength in Angstroms for segment A of setting G130M/1291/FUVA, using combinations of 2 FP-POS. The different colors correspond to different combinations of 2 FP-POS (blue = 1+2; red = 1+3; black = 1+4; green = 2+3; cyan = 2+4; magenta = 3+4). The smoother, dashed line lying above the solid line in each panel indicates the Poisson S/N computed from the error array of *x1dsum* files.

With G160M, users can expect to reach S/N of 22, 28, and 32 with 2, 3, and 4 FP-POS, respectively. With G140L, a S/N of 23, 29, and 36 can be reached with 2, 3, and 4 FP-POS.

4. Summary and Conclusion

In this ISR, we determined the maximum achievable S/N, $(S/N)_{max}$, as a function of the number of FP-POS included in COS spectra for each segment and cenwave of the G130M, G160M, adn G140L gratings using deep calibration observations aimed at measuring the two-dimensional spectral profiles of the different COS settings. $(S/N)_{max}$ is limited by fixed pattern noise on the COS detectors. We found that $(S/N)_{max}$ increases as the number of FP-POS used increases, which is expected given that fixed pattern noise will average out using spectral dithers. $(S/N)_{max}$ also varies with wavelength (i.e., across

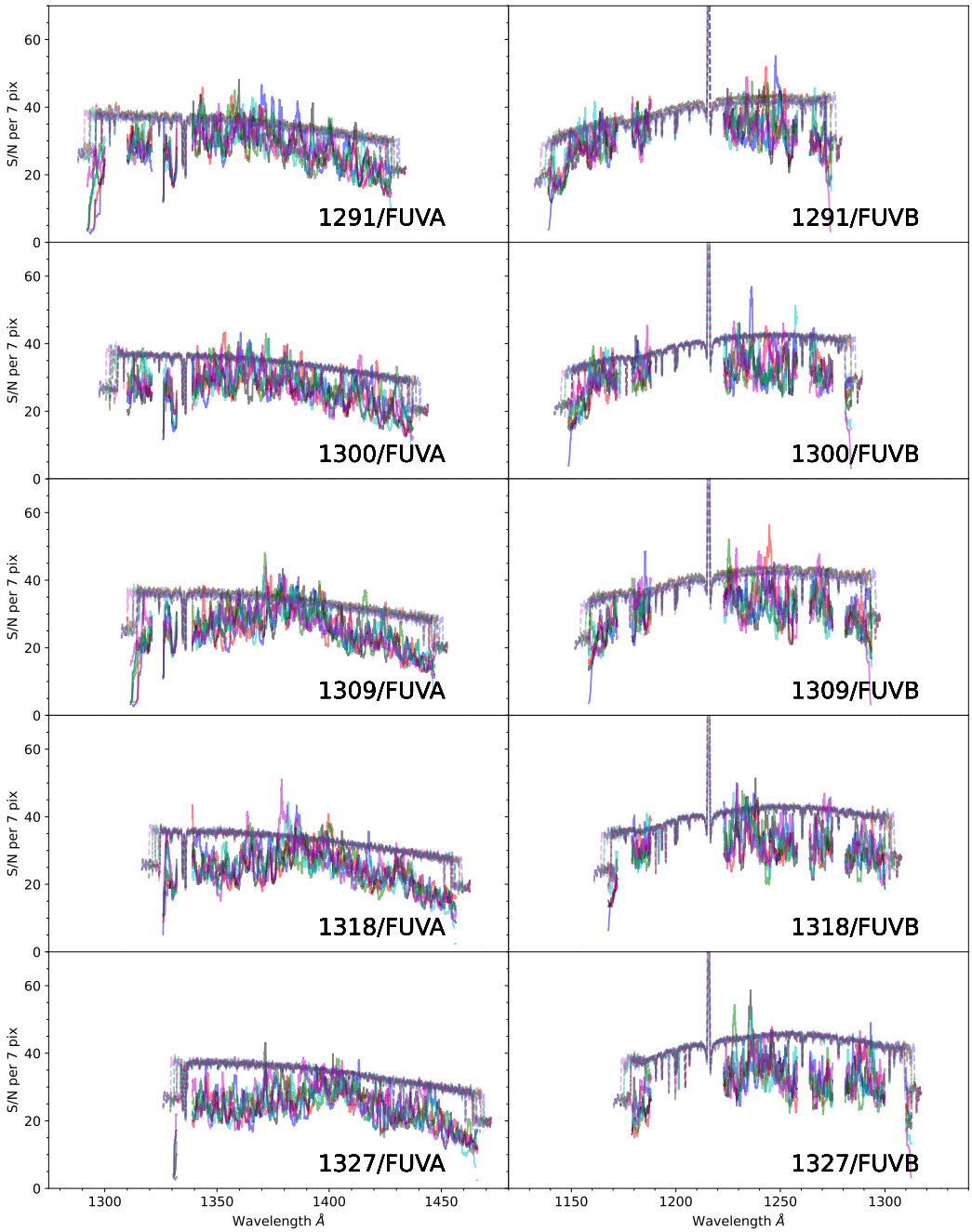

Figure 3. Empirical (effective) S/N per 7 pixel resel as a function of wavelength in Angstroms for segment A (left) and segment B (right) of cenwaves 1291, 1300, 1309, 1318 and 1327 (top to bottom) for the G130M grating, using combinations of 2 FP-POS. The different colors correspond to different combinations of 2 FP-POS (blue = 1+2; red = 1+3; black = 1+4; green = 2+3; cyan = 2+4; magenta = 3+4). The smoother, dashed line lying above the solid line in each panel indicates the Poisson S/N computed from the error array of *x1dsum* files.

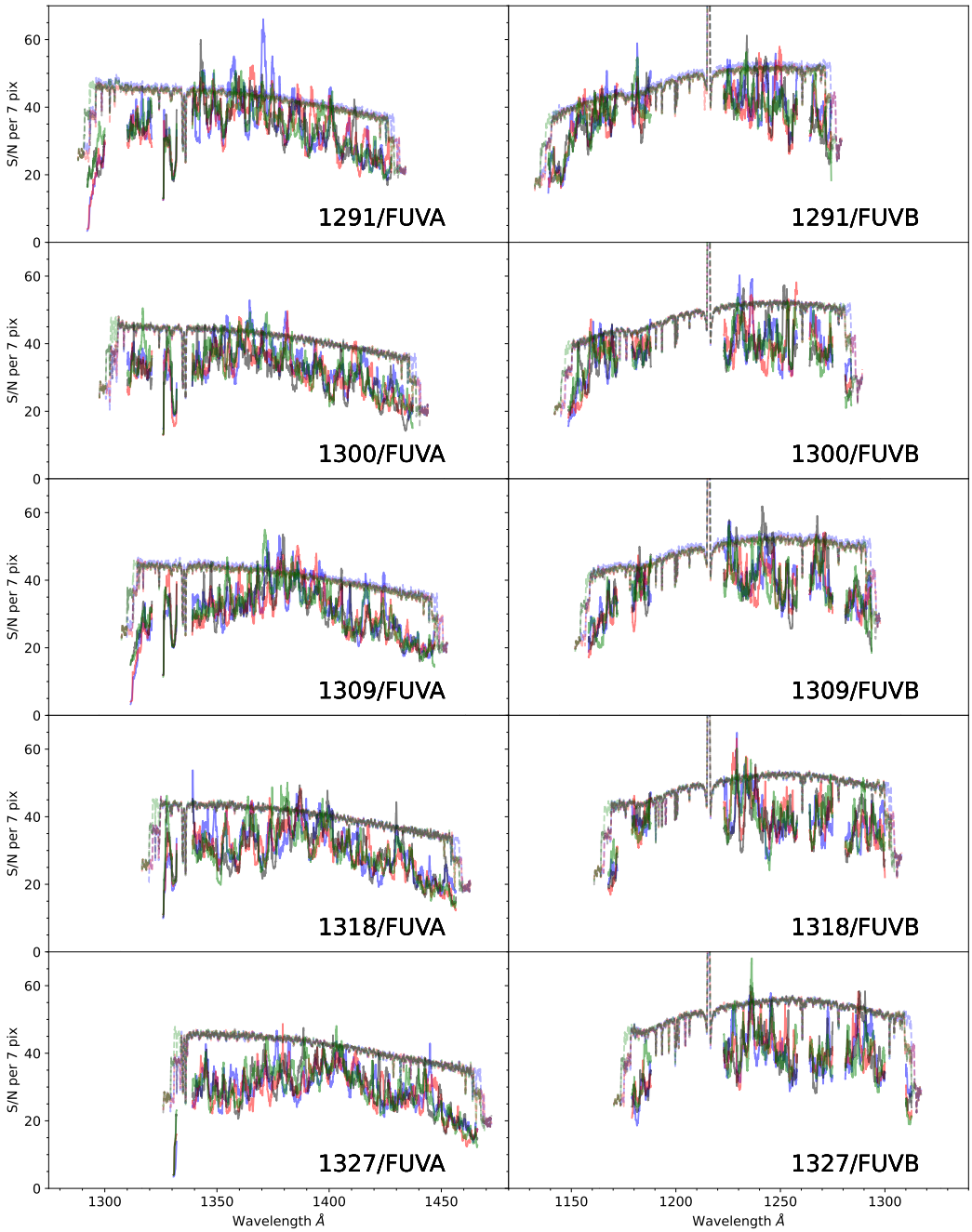

Figure 4. Empirical (effective) S/N per 7 pixel resel as a function of wavelength in Angstroms for segment A (left) and segment B (right) of cenwaves 1291, 1300, 1309, 1318 and 1327 (top to bottom) for the G130M grating, using combinations of 3 FP-POS. The different colors correspond to different combinations of 3 FP-POS (blue = 1+2+3; red = 1+2+4; black = 1+3+4; green = 2+3+4). The smoother, dashed line lying above the solid line in each panel indicates the Poisson S/N computed from the error array of *x1dsum* files.

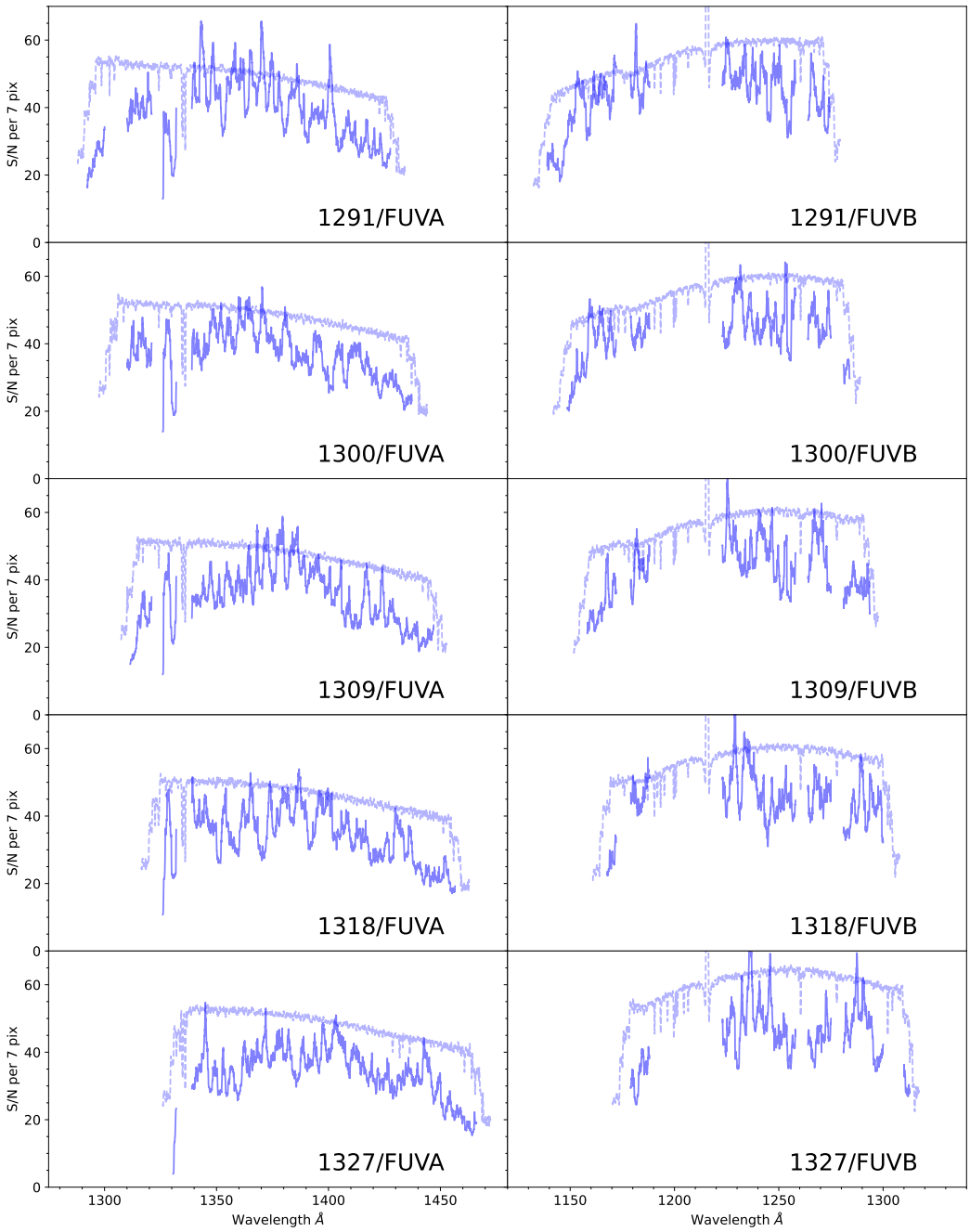

Figure 5. Empirical (effective) S/N per 7 pixel resel as a function of wavelength in Angstroms for segment A (left) and segment B (right) of cenwaves 1291, 1300, 1309, 1318 and 1327 (top to bottom) for the G130M grating, using all 4 FP-POS. The smoother, dashed line lying above the solid line in each panel indicates the Poisson S/N computed from the error array of *x1dsum* files.

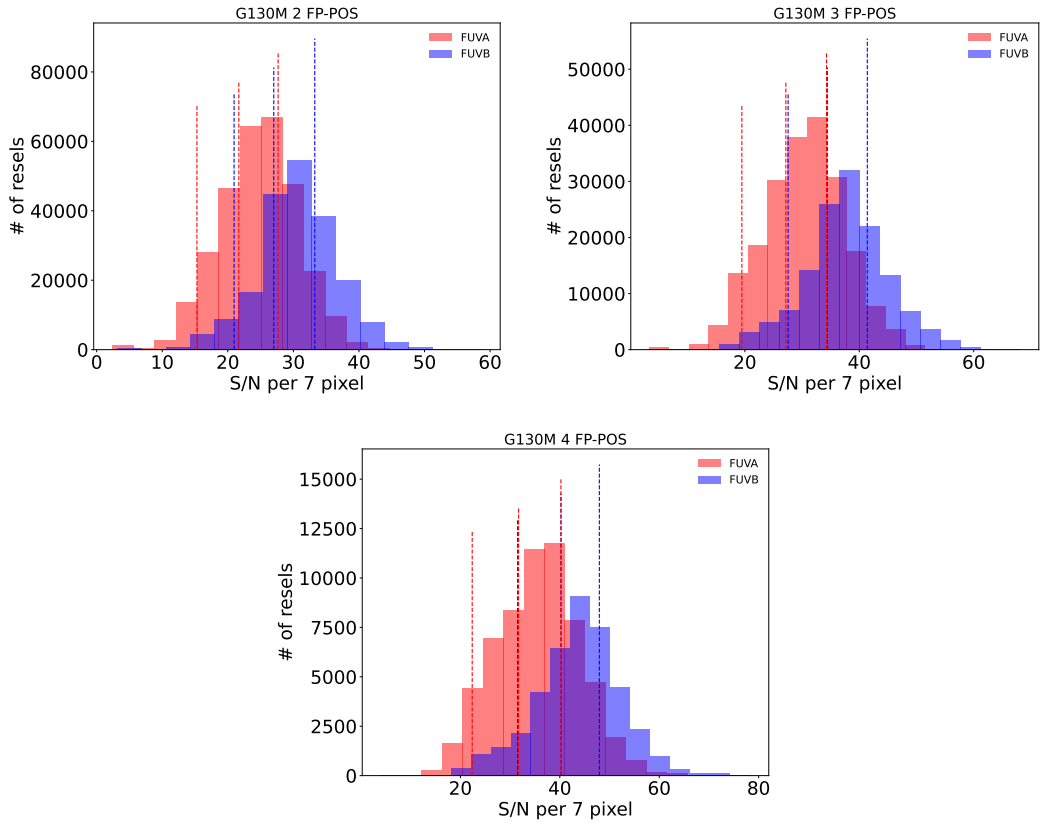

Figure 6. Histogram of the empirical (effective) S/N per 7 pixel resel for segment A (red) and segment B (blue) for G130M and combinations of 2 (top left), 3 (top right), and 4 (bottom) FP-POS. Data are combined for all cenwaves (1291, 1300, 1309, 1318 and 1327). The vertical dashed lines indicate the $16^{\rm th}$, $50^{\rm th}$, and $84^{\rm th}$ percentiles for each segment.

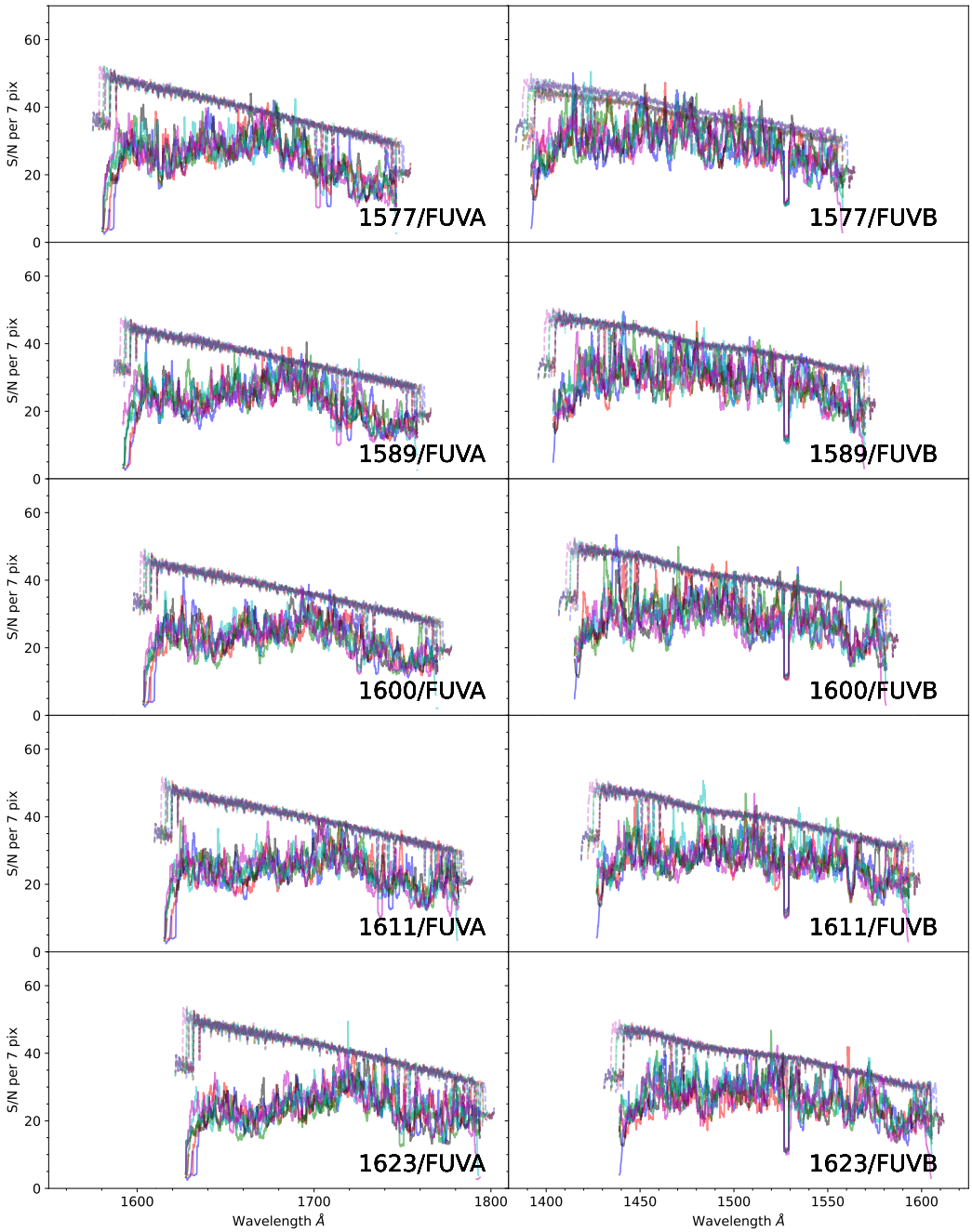

Figure 7. Empirical (effective) S/N per 7 pixel resel as a function of wavelength in Angstroms for segment A (left) and segment B (right) of cenwaves 1577, 1589, 1600, 1611, and 1623 (top to bottom) for the G160M grating, using combinations of 2 FP-POS. The different colors correspond to different combinations of 2 FP-POS (blue = 1+2; red = 1+3; black = 1+4; green = 2+3; cyan = 2+4; magenta = 3+4). The smoother, dashed line lying above the solid line in each panel indicates the Poisson S/N computed from the error array of *x1dsum* files.

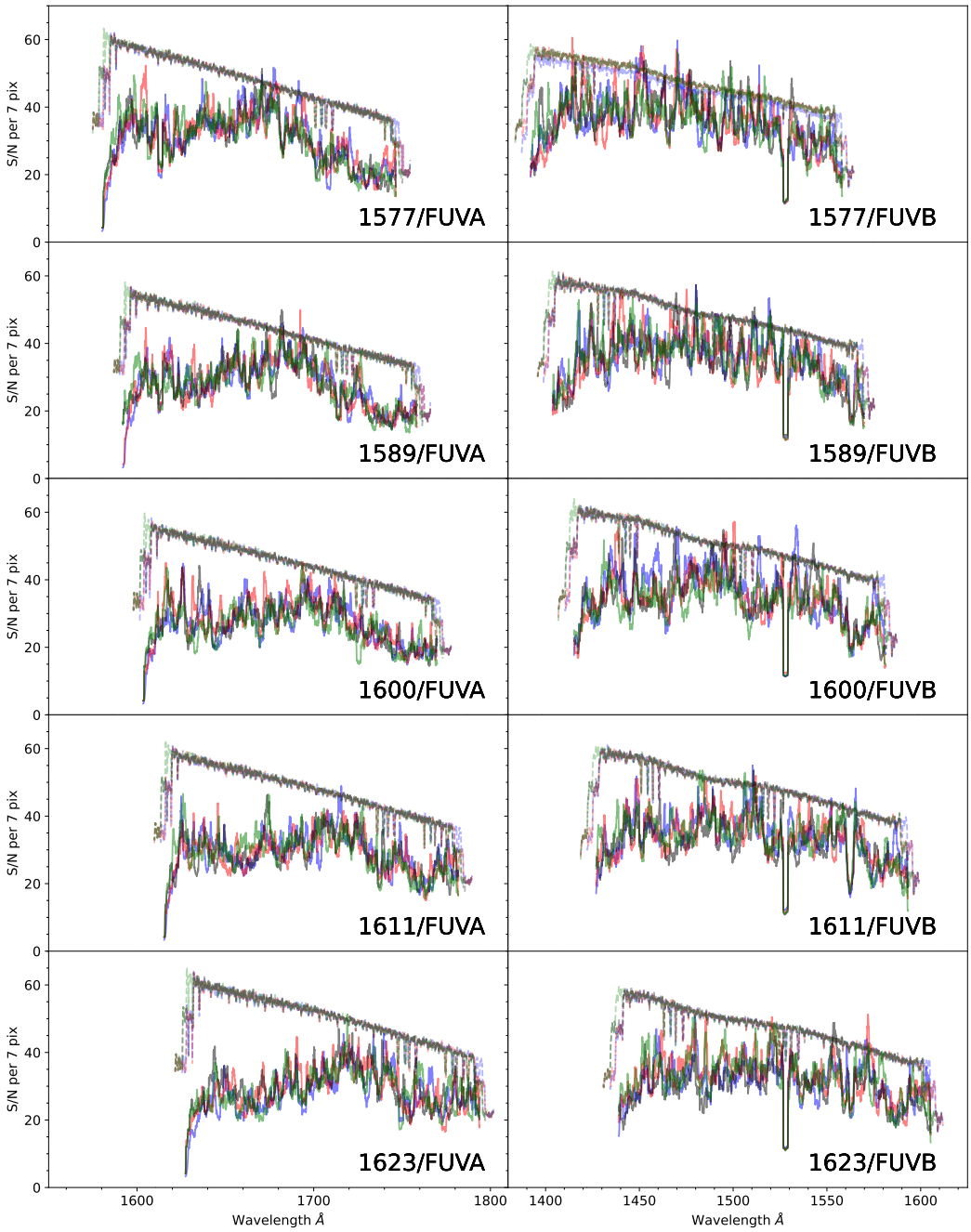

Figure 8. Empirical (effective) S/N per 7 pixel resel as a function of wavelength in Angstroms for segment A (left) and segment B (right) of cenwaves 1577, 1589, 1600, 1611, and 1623 (top to bottom) for the G160M grating, using combinations of 3 FP-POS. The different colors correspond to different combinations of 3 FP-POS (blue = 1+2+3; red = 1+2+4; black = 1+3+4; green = 2+3+4). The smoother, dashed line lying above the solid line in each panel indicates the Poisson S/N computed from the error array of *x1dsum* files.

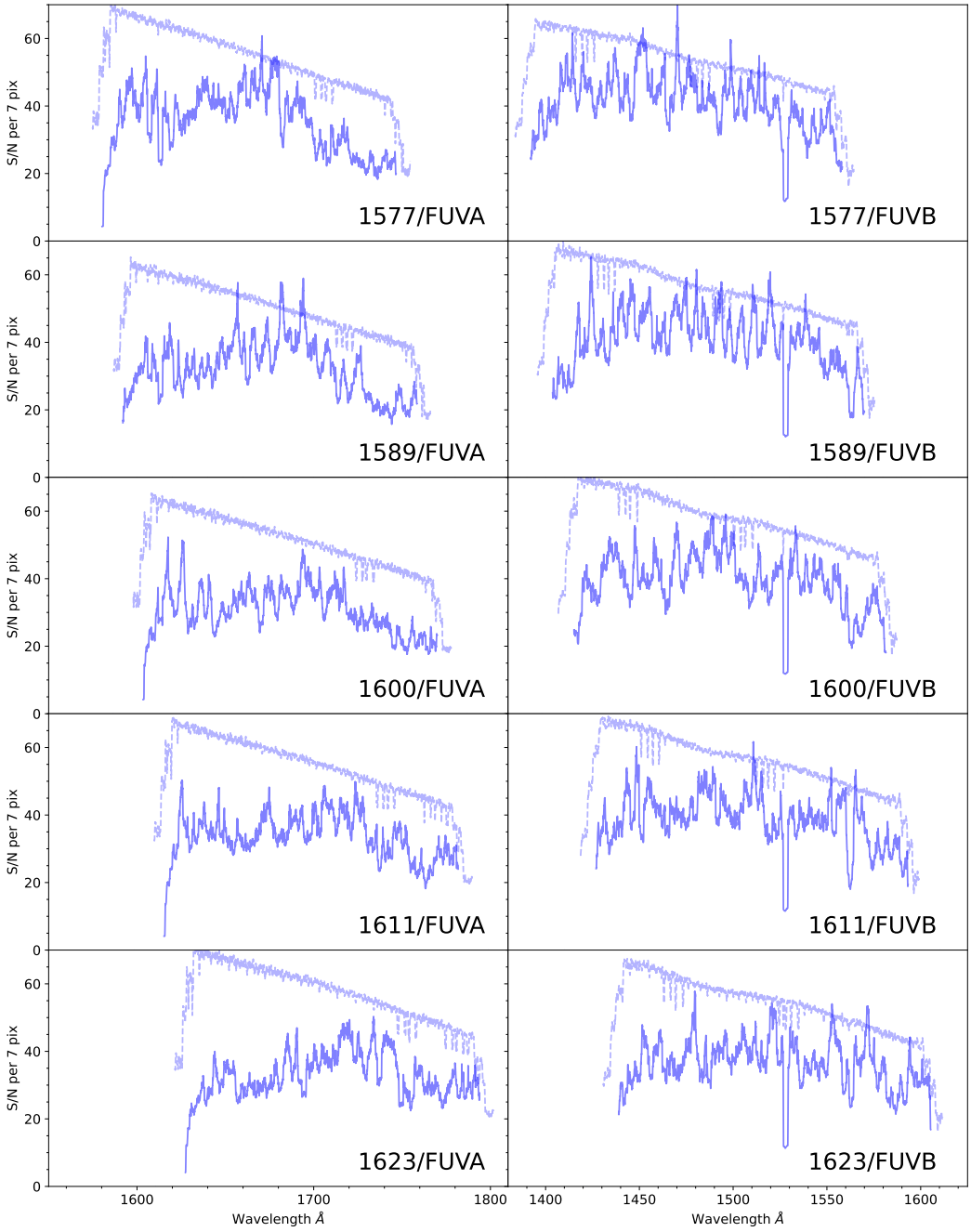

Figure 9. Empirical (effective) S/N per 7 pixel resel as a function of wavelength in Angstroms for segment A (left) and segment B (right) of cenwaves 1577, 1589, 1600, 1611, and 1623 (top to bottom) for the G160M grating, using all 4 FP-POS. The dashed line at the top of each panel indicates the Poisson S/N computed from the error array of *x1dsum* files.

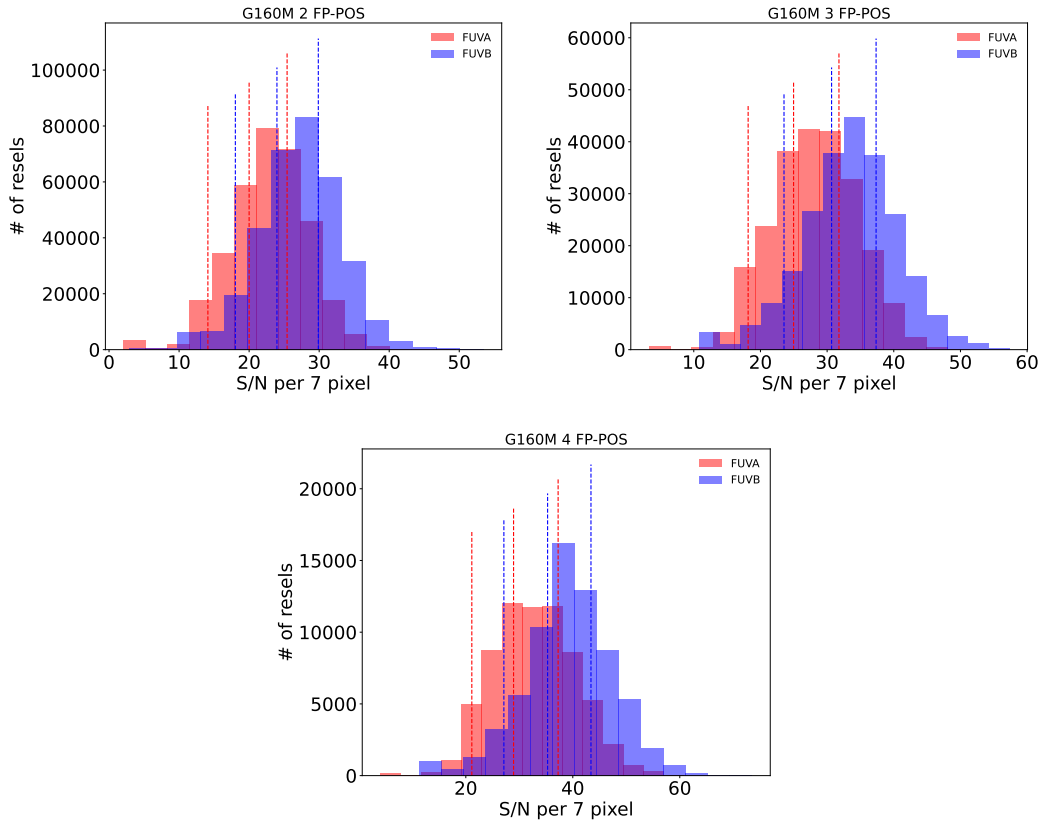

Figure 10. Histogram of the empirical (effective) S/N per 7 pixel resel for segment A (red) and segment B (blue) for G130M and combinations of 2 (top left), 3 (top right), and 4 (bottom) FP-POS. Data are combined for all cenwaves (1577, 1589, 1600, 1611, and 1623). The vertical dashed lines indicate the $16^{\rm th}$, $50^{\rm th}$, and $84^{\rm th}$ percentiles for each segment.

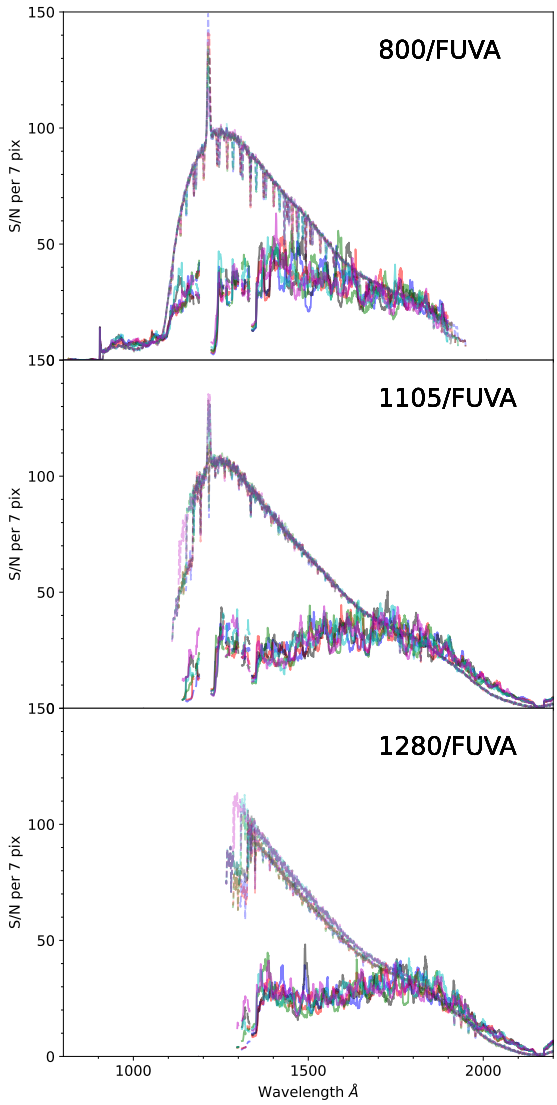

Figure 11. Empirical (effective) S/N per 7 pixel resel as a function of wavelength in Angstroms for segment A of cenwaves 800, 1105, and 1280 (top to bottom) for the G140L grating, using combinations of 2 FP-POS. The different colors correspond to different combinations of 2 FP-POS (blue = 1+2; red = 1+3; black = 1+4; green = 2+3; cyan = 2+4; magenta = 3+4). The smoother, dashed line lying above the solid line in each panel indicates the Poisson S/N computed from the error array of *x1dsum* files.

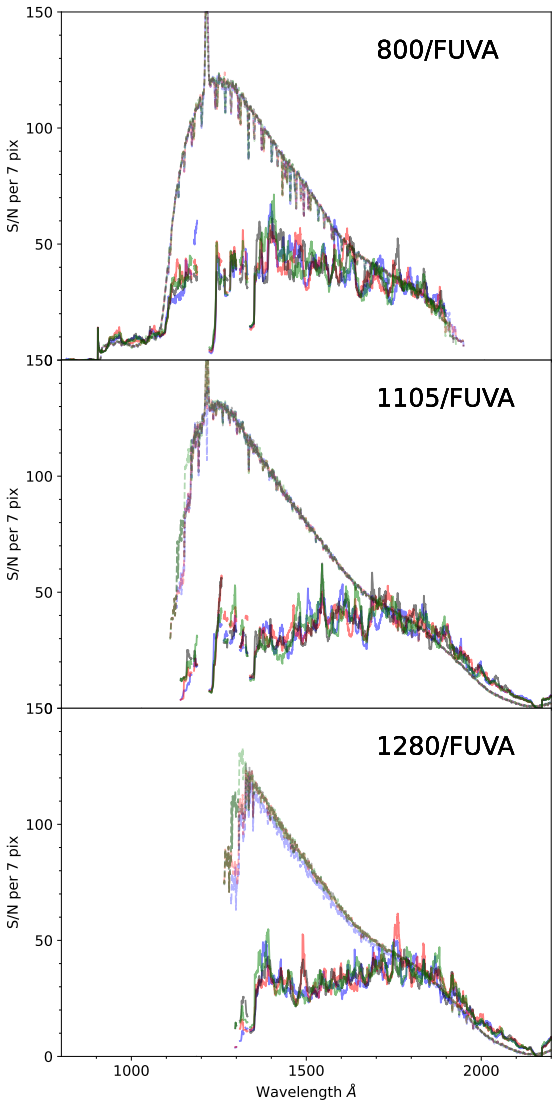

Figure 12. Empirical (effective) S/N per 7 pixel resel as a function of wavelength in Angstroms for segment A of cenwaves 800, 1105, and 1280 (top to bottom) for the G140L grating, using combinations of 2 FP-POS. The different colors correspond to different combinations of 3 FP-POS (blue = 1+2+3; red = 1+2+4; black = 1+3+4; green = 2+3+4). The smoother, dashed line lying above the solid line in each panel indicates the Poisson S/N computed from the error array of *x1dsum* files.

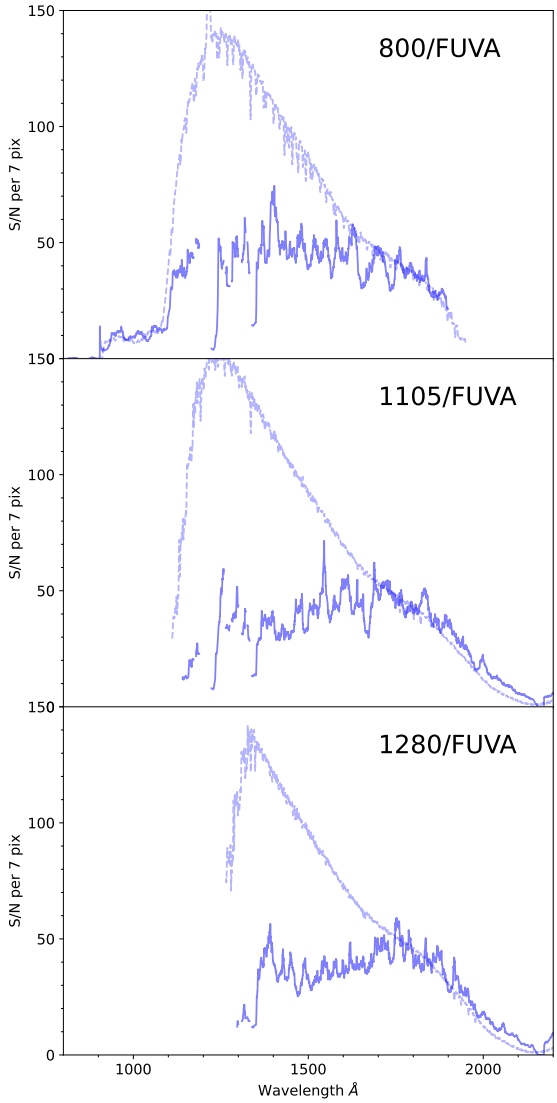

Figure 13. Empirical (effective) S/N per 7 pixel resel as a function of wavelength in Angstroms for segment A of cenwaves 800, 1105, and 1280 (top to bottom) for the G140L grating, using all 4 FP-POS. The smoother, dashed line lying above the solid line in each panel indicates the Poisson S/N computed from the error array of *x1dsum* files.

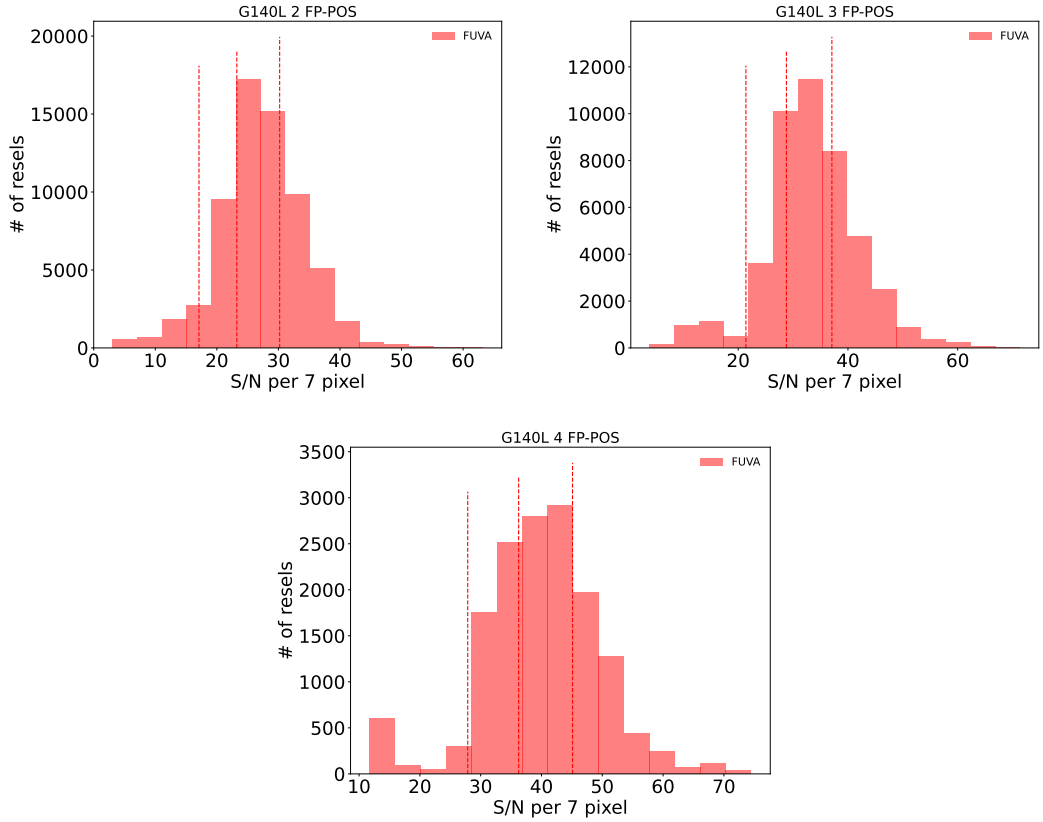

Figure 14. Histogram of the empirical (effective) S/N per 7 pixel resel for segment A for G140L and combinations of 2 (top left), 3 (top right), and 4 (bottom). Data are combined for all cenwaves (800, 1105, and 1280). The vertical dashed lines indicate the $16^{\rm th}$, $50^{\rm th}$, and $84^{\rm th}$ percentiles.

a segment), grating, and cenwave. This variation is driven by variations in the width of the cross-dispersion profile. For settings or detector regions with wider cross-dispersion profiles, the fixed pattern noise is averaged over a larger number of two-dimensional pixels, resulting in a lower level of fixed pattern noise in extracted, one-dimensional spectra. With G130M, users can reach S/N of about 25, 30, and 35 with 2, 3, and 4 FP-POS, respectively. With G160M, users can expect to reach S/N of 22, 28, and 32 with 2, 3, and 4 FP-POS, respectively. And with G140L, the approximate achievable S/N is 23, 29, and 36 with 2, 3, and 4 FP-POS. This investigation is based on data obtained at LP3. Cross-dispersion profiles are expected to increase slightly with distance from LP1, which might in turn increase $(S/N)_{max}$ away from LP1. However, we do not expect this increase to be large.

5 Change History for COS ISR 2023-11

Version 1: May 18, 2023- Original Document

References

Ake, T.B., et al., 2010, 2010 Space Telescope Science Institute Calibration Workshop - Hubble after SM4. Edited by Susana Deustua and Cristina Oliveira.
COS FUV Flat Fields and Signal-to-Noise Characteristics

Hasselquist, S., et al., 2023, Instrument Science Report COS ISR 2023-??: *TBD*

James, B., et al., 2023, Instrument Science Report COS ISR 2023-???: *TBD*

Oliveira, C., et al., 2013, COS ISR 2013-02: *COS/FUV Mapping of Stray PtNe Lamp Light Through the FCA*

Oliveira, C., et al., 2018, COS ISR 2018-16: *COS2025: A New Strategy to Prolong the Lifetime of the COS/FUV Detector to 2025*

Osterman, S., et al. 2011, Ap&SS, 335, 257: *The Cosmic Origins Spectrograph: on-orbit instrument performance*

Proffitt, C., et al., 2015, COS ISR 2015-03: *Changes to the COS Extraction Algorithm for Lifetime Position 3*

Rafelski, M., et al., 2018, COS ISR 2018-21: *Traces, Profiles, and Extraction Tables for the COS FUV Channel at Lifetime Position 4*

Roman-Duval, J., et al, 2017, COS ISR 2017-06: *Spectral Resolution of COS/FUV at Lifetime Position 3*